INNSPUB

Journal of Biodiversity and Environmental Sciences | JBES
ISSN: 2220-6663 (Print); 2222-3045 (Online)
Website: https://www.innspub.net
E-mail contact: info@innspub.net
Vol. 29, Issue: 2, p. 53-66, 2026

RESEARCH PAPER

OPEN ACCESS

A minor Ivorian-Ghanian upwelling season influenced by the interaction between the Atlantic El Niño and marine heat waves

Mamadou Koné*[1], Hilaire Amemou[1], Kouakou Urbain Koffi[1,3], Yves Kouadio[2]

[1]*Training and Research Unit of Marine Sciences, University of San-Pédro, San-Pédro, Cote d'Ivoire*

[2]*Laboratory of Matter Sciences, Environment and Solar Energy (LASMES), University F.H.B. of Cocody-Abidjan, Abidjan, Cote d'Ivoire*

[3]*Department of Science and Technology, École Normale Supérieure, Abidjan, Côte d'Ivoire*

Key words: Upwelling, Gulf of Guinea, Atlantic Niño, Marine heatwave, Interannual variability, Causal analysis

Received: 22 July, 2026 **Accepted:** 01 August, 2026 **Published:** 08 August, 2026

DOI: https://dx.doi.org/10.12692/jbes/29.2.53-66

ABSTRACT

This study examines the spatio-temporal variability of coastal upwelling in the northern Gulf of Guinea during the minor upwelling season (January–February) between 1993 and 2025, and analyses its relationship with the Atlantic El Niño phenomenon and marine heatwaves. Sea surface temperature data reveal two distinct upwelling centres (Cape Palmas and Cape Three Points). The western cell exhibits high interannual variability, with an extreme event in 1996, but no significant trend. In contrast, the eastern cell shows a significant downward trend, with a regime shift between 2006 and 2007. Analysis of marine heatwaves shows that they are almost exclusively concentrated after 2017, with a record intensity in 2024 (33.9 °C d). Their cumulative intensity is associated with a significant upward trend (slope= +0.2965 °C d/year). Bivariate analyses of the Atlantic El Niño phenomenon, marine heatwaves and the deep-water upwelling area reveal significant negative correlations. However, a multiple regression identifies the Atlantic El Niño as the main factor reducing upwelling, whilst the direct effect of marine heatwaves is not significant. These results highlight contrasting trends within upwelling cells, the recent emergence of intense marine heatwaves, and the dominant role of the Atlantic Niño in modulating the intensity of upwelling in the region.

***Corresponding Author:** Mamadou Koné ✉ konemamadou884@gmail.com

INTRODUCTION

The Gulf of Guinea (GoG), and more specifically the Ivorian-Ghanaian coastal section, constitutes a major ecosystem within the Guinea Current Large Marine Ecosystem (GCLME), characterised by exceptional primary productivity (Nubi *et al.*, 2019). This system does not exhibit the dynamics of permanent upwelling, such as the Canary Current, but rather a binary seasonal pattern, with a major summer upwelling season and a minor winter upwelling season, the functioning of which is intrinsically linked to more complex mechanisms (Djakouré *et al.*, 2014; Houghton, 1989). The minor upwelling, although less intense than its summer counterpart, plays a crucial role in sustaining fish stocks (Hardman-Mountford and McGlade, 2003). Its dynamics are based on a fragile thermodynamic equilibrium, namely Ekman transport, driven by trade winds, which must be sufficient to break the surface stratification and allow cold, nutrient-rich water to rise into the euphotic zone (Bakun, 1978). However, recent oceanographic observations reveal that this system is increasingly less governed by local processes (Koné *et al.*, 2022). It is now subject to large-scale atmospheric and oceanic forcings that call into question the long-term predictability of this phenomenon. Among these forcings, Atlantic Niño appears to be a key moderator (Brandt *et al.*, 2023). Through eastward-propagating equatorial Kelvin waves, this phenomenon alters the depth of the thermocline across the basin, mechanically inhibiting the potential for deep-water upwelling, even in the presence of favourable wind conditions (Imbol Koungue *et al.*, 2017; Jouanno *et al.*, 2017). Indeed, the interannual variability of the major cold season is also exacerbated by the increasing frequency of Marine Heatwaves (MHWs; Djakouré *et al.*, 2023; Koné *et al.*, 2022, 2025). MHW events are defined as periods of extreme temperature anomalies exceeding the 90th percentile of the local climate record (Hobday *et al.*, 2016). According to studies by Wernberg (2021) and Oliver *et al.* (2018), MHWs sharply intensify surface thermal stratification, acting as a barrier that prevents vertical mixing, which severely limits the availability of nutrients and, by extension, primary production. This convergence of distant climatic disturbances, such as the Atlantic El Niño, and localised thermal anomalies, such as MHWs, represents a break with the long-established functioning of upwelling systems (Oliver *et al.*, 2019). Furthermore, the synergy between these two stressors lies in the fact that the former affects the depth of the thermocline whilst the latter affects surface stratification, creating an unprecedented state of ecosystem stress.

This study aims to explore these dynamics of dysfunction by examining how the coupling between the Atlantic El Niño and MHWs redefines the instability of the Ivorian-Ghanian minor upwelling season. Using the approach outlined by Caniaux *et al.* (2011), we will analyse the interannual evolution of this system; subsequently, based on the method described by Hobday *et al.* (2016) we will assess whether the climatic shift between the Atlantic El Niño and the MHWs is causing an irreversible alteration to the resilience of these coastal ecosystems.

MATERIALS AND METHODS

Study area

The northern coast of the GoG studied in this paper is bounded to the west by 10°W and to the east by 2.5°E, and lies within the latitudinal band between 3.5°N and 6°N (Fig. 1). It forms part of the eastern tropical Atlantic Ocean. It is a region of great oceanographic interest due to the seasonal upwelling of nutrient-rich deep water to the surface (Kouadio *et al.*, 2013). This coastal upwelling, which extends for nearly 1,000 km from Côte d'Ivoire to Nigeria, has two distinct seasons: a major upwelling during the northern hemisphere summer (June to September), characterised by a drop of several degrees in surface temperature, and a smaller, more moderate upwelling in January-February (Djakouré *et al.*, 2014).

Data

To calculate the upwelling area, its index and the MHWs in this study, we used temperature data from 1993 to 2025 derived from the Copernicus Marine Environment Monitoring Service's global ocean

reanalysis (product GLOBAL_MULTIYEAR_PHY_001_030, data set cmems_mod_glo_phy_my_0.083deg_P1D-m) at 5 m. These daily mean data fields are based on the MERCATOR GLORYS12V1 configuration from Mercator Ocean, which provides a global simulation at a high spatial resolution of 1/12° (approximately 8 km). These data were extracted via the Marine Data Store's MyOcean portal from the Copernicus Marine Service's Global Ocean Physics Reanalysis Copernicus Marine Service. They have been the subject of several studies in the Atlantic, such as those by Song and Aiki (2023) , and are adequately described in this oceanic region by the work of Jean-Michel *et al.* (2021). Data for the ATL3 index were used from 1993 to 2025 during the months of January and February. This index is defined as the SST anomaly in the equatorial Atlantic region bounded by 3°S-3°N and 20°W-0°E, with positive and negative periods based on a threshold of ±0.4°C. These data are available via the following link:
https://www.cpc.ncep.noaa.gov/products/international/ocean_monitoring/IODMI/rATL3.html.
They have previously been used by Tan *et al.* (2023) to study the multi-temporal variation of the Atlantic Niño.

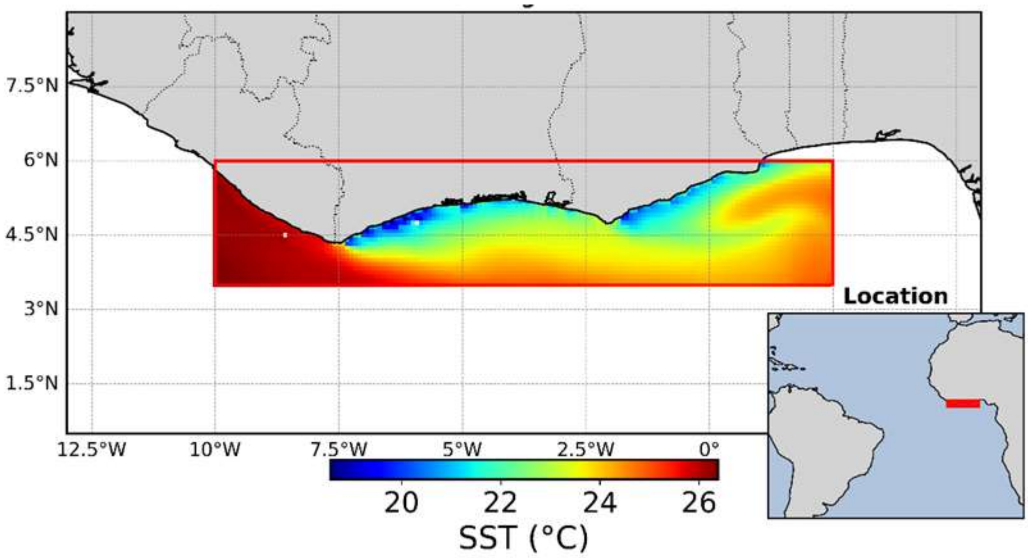

Fig. 1. The northern coast of the Gulf of Guinea (outlined in red), bounded by 10°W and 2.5°E and by 3.5°N and 6°N, located in the eastern tropical ocean, showing the average sea surface temperature (SST) observed on 12 August 2012

Calculation of the upwelling area and the upwelling index

To calculate the upwelling area and the upwelling index, the method developed by Caniaux *et al.* (2011) was used. This method involves integrating, on a daily basis, the area of all grid cells where the SST is below a predefined threshold value, using the formula below. This temperature threshold is set at 26 °C, a characteristic value chosen from the study by Demarcq and Aman (2002), in which the authors used this threshold to calculate the area of coastal upwelling off the northern coast of the Gulf of Guinea. However, prior to application, our study area was subdivided into two zones corresponding to distinct upwelling cells. These are the western cell associated with Cape Palmas (Liberia/Côte d'Ivoire) and the eastern cell associated with Cape Trois Pointes (Ghana). This division is based on coastal geography and regional wind dynamics. Furthermore, the upwelling index was calculated as the ratio, expressed as a percentage, of the daily upwelling area to the total ocean area of the cell in question (Caniaux *et al.*, 2011). This index thus represents the fraction of the cell covered by cold water (< 26 °C). To assess the degree of temporal coherence between the two upwelling cells, a Pearson correlation coefficient was calculated between the annual time series of the relative indices for the western and eastern cells. A significantly positive correlation ($p < 0.05$) indicates that the two cells evolve synchronously, whilst a weak or non-significant correlation suggests independent dynamics or dynamics governed by distinct forcings.

Detection of MHWs

MHWs were detected using the method developed by Hobday *et al.* (2016). This method is based on the definition of a reference climatology and a variable threshold calculated on a day-by-day basis. In this study, the climatology covers the entire period 1993-2025 for the months of January and February. For each day of the year, the reference temperature is the 90th percentile of the temperatures observed on that date over the entire period, smoothed using a 31-day moving average (Hobday *et al.*, 2016). The alert threshold is defined as the value of this percentile. A day is classified as an MHW if the SST exceeds the climatological threshold for that day. Episodes are defined as continuous sequences of at least five consecutive days on which the threshold is exceeded. Gaps of up to 2 days are filled in to form coherent events (Hobday *et al.*, 2016). This method has been used on several occasions in this study area (Djakouré *et al.*, 2023; Koné *et al.*, 2022, 2025). The cumulative intensity of MHWs for the January-February season is simply the sum of the intensities calculated by taking the difference between the temperature on MHW days and the threshold. It represents the cumulative excess heat (in °C.days) during MHWs episodes over the January-February season.

Statistical tests

To assess whether there is a break in the trend of the upwelling index, Pettitt's break test was applied. This is a non-parametric test that detects an abrupt change in the mean of a time series.

It identifies the most likely year of the break and calculates the means before and after this point (Xie *et al.*, 2014). Significance is assessed using a Monte Carlo method with 20.000 simulations.

The test returns the significance of the break ($p < 0.05$), the years flanking the break, and the means of the two regimes before and after (Mallakpour and Villarini, 2016). Furthermore, to assess the temporal evolution of cumulative intensity over the period 1993-2025 during January and February, two approaches were applied. These are the linear trend test using ordinary least squares (OLS) regression and the Mann-Kendall trend test. Applying OLS to the time series yields the trend slope (in °C.day per year), Pearson's correlation coefficient (r) and the associated p-value, which indicates the statistical significance of the trend (Stock and Watson, 2017; Wooldridge, 2016). The non-parametric Mann-Kendall test is used in conjunction with linear regression. Unlike the OLS approach, this test is robust to outliers and does not assume a normal distribution of the residuals (Hipel and McLeod, 1994). It detects monotonic trends regardless of whether they are linear or not. This test returns the direction of the trend ("increasing", "decreasing" or "no trend"), significance ($p < 0.05$), Kendall's correlation coefficient (τ) and Sen's slope, which provides a robust estimate of the magnitude of the trend (in °C.day per year, Hipel and McLeod, 1994).

Causality via convergent cross mapping

To assess the causal link between MHWs, the Atlantic Niño and the decline in upwelling, we used the Convergent Cross Mapping (CCM) method (Sugihara *et al.*, 2012). This non-parametric approach is well-suited to non-linear ocean systems, as it detects causal relationships without requiring an explicit mechanistic model (Sugihara *et al.*, 2012). Its principle is based on the idea that if a variable X influences Y, then the imprint of X is contained within the attractor reconstructed from Y (Osada *et al.*, 2023). In this study, we reconstructed the upwelling attractor using time-delay embedding, with a fixed dimension of 3, in order to predict the presumed causal variables (MHW or El Niño in the Atlantic, or both). The quality of the prediction was quantified using Pearson's correlation coefficient (ρ) between the predicted and observed values. To validate causality, we carried out a convergence analysis by varying the size of the library (L).

For each value of L, the mean value of ρ was calculated from 200 bootstrap resamples. A genuine causal link requires that ρ increases with L (Runge *et al.*, 2019). We therefore tested the correlation between L and the mean ρ (L). A positive and significant correlation ($p < 0.05$) confirms that the MHWs or the Atlantic Niño, or both, exert a causal effect on the reduction in upwelling.

RESULTS

Spatial and temporal climatology of the two upwelling cells

The climatology of observed SST during the minor upwelling season (January-February, 1993-2025) reveals a cold thermal signature along the northern coast of the GoG (Fig. 2a). The spatial division established at the longitude of Cape Three Points, approximately -2.083°W, allows two dynamically distinct sub-regions to be distinguished. These are the Western cell (Cape Palmas) cell, extending between 10°W and -2.083°W and characterised by an extensive core of cold water along the Ivorian-Liberian coast, and the Eastern (Cape Three Points) cell, extending east of -2.083°W and covering the Ghanaian, Togolese and Beninese continental shelves. Surface water temperatures show minimum average values of less than 27°C in both cells, confirming the existence of two centres of coastal cold-water inflow. The interannual variability in the upwelling area shown in Fig. 2b indicates that the western cell (blue curve) is characterised by high interannual variability, marked by an extreme event observed in 1996. This event is characterised by an exceptional positive anomaly, with a cumulative upwelling area exceeding 1.5×10^6 km²·days and an average index reaching 17.3% (Fig. 2b). The year 2012 was also a cold year, with a value of approximately 0.75×10^6 km²·days. In contrast, the years 1994, 1998, 2010, 2011, 2013 and 2020 did not experience any cooling during the January-February period. The OLS linear trend applied to the cumulative area indicates a negative trend of 7.967 km²·day/year, with statistical stability at p = 0.157. Furthermore, the non-parametric Mann-Kendall test applied to the upwelling index time series (Fig. 2b) shows no statistically significant trend for the average index, with τ = -0.07, p = 0.556 and Sen's slope = -0.0106%/year. The Pettitt test applied to the upwelling index (Fig. 2c) identifies a potential point of change between 2007 and 2008, but this break remains insignificant with p = 0.667. Thus, the average index decreases by 2.95% before and by 1.47% after. Observation of the Fig. 2b for the Eastern cell shows a smaller cooling area than that of the Western cell and a very different temporal behaviour, characterised by a gradual decline Observation of the Fig. 2b for the Eastern cell shows a smaller cooling area than that of the Western cell and a very different temporal behaviour, characterised by a gradual decline. The largest upwelling area observed in this cell was in 2012, with an area of approximately 0.4106 km²·days. Unlike the western cell, the eastern cell has experienced a high number of warm years: 1994, 1998, 2002, 2008, 2010, 2011, 2013, 2015-2020 and 2023-2025, associated with a cumulative upwelling area, is experiencing an average decline of -3.559 km² days per year, with p = 0.034. Indeed, application of the Mann-Kendall test (Fig. 2b) reveals a statistically significant downward trend in the upwelling index, with τ= -0.32, p = 0.009 and a Sen slope of -0.0295% per year. At the same time, the Pettitt test confirms a statistically significant regime shift between 2006 and 2007 with p = 0.014 (Fig. 2d).

Following this regime shift in 2006/2007, the average upwelling index for the Eastern cell fell by more than half, dropping from 1.57% during the period 1993-2006 to 0.68% during the period 2007-2025.

Variability of MHWs and the Atlantic Niño during the January–February period from 1993 to 2025

Analysis of the cumulative intensity of MHWs during the January–February period between 1993 and 2025 (Fig. 3) reveals high interannual variability characterised by marked temporal asymmetry. Over the 33-year observation series, only 8 years recorded MHW events meeting the detection criteria of Hobday *et al.* (2016). Between 1993 and 2016, MHW activity during the January–February window remained very marginal, with cumulative anomalies above the 90th percentile remaining close to zero. In contrast, the recent period (2017-2025) is characterised by the concentration of almost all major events. Indeed, the year 2024 represents the peak of the time series, recording a record cumulative intensity value of 33.9 °C.day. Next, the year 2020 represents the second most intense event observed, with a cumulative total of 20.86 °C.day. The years 2017, 2022 and 2025 also show significant MHW activity, confirming the recent recurrence of these temperature anomalies.

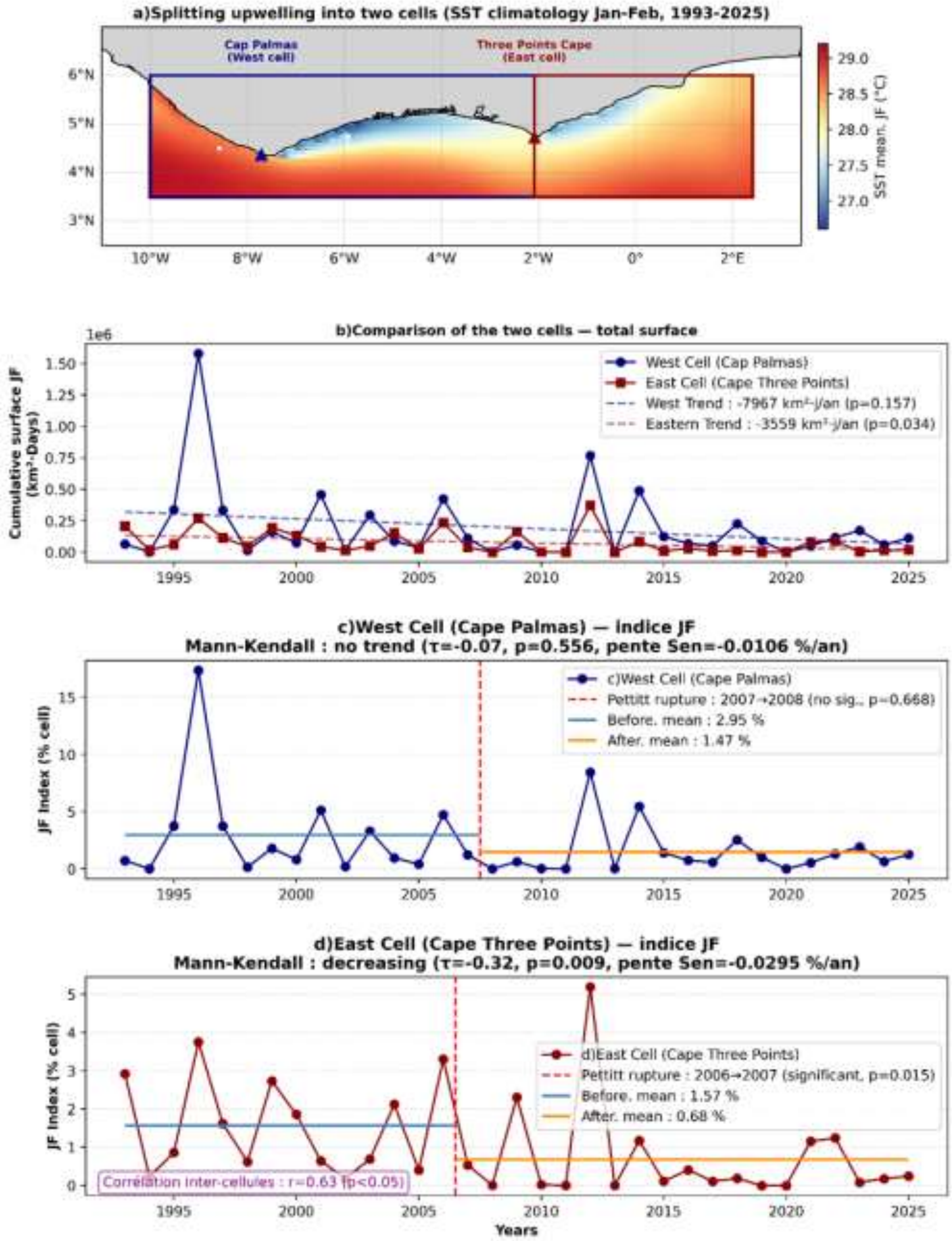

Fig. 2. (a) Spatial structure of the two upwelling cells (the western cell outlined in blue and the eastern cell outlined in red), (b) the temporal evolution of the area of the two cells (the blue curve corresponds to the area of the western cell and the red curve to that of the eastern cell), with the dotted lines representing the trends of the two curves, (c, d) the temporal variations in the upwelling indices of the different cells (curve c corresponds to the western cell and d to the eastern cell)

The blue and orange lines represent the averages of these indices before and after the break indicated by the red dotted lines, respectively.

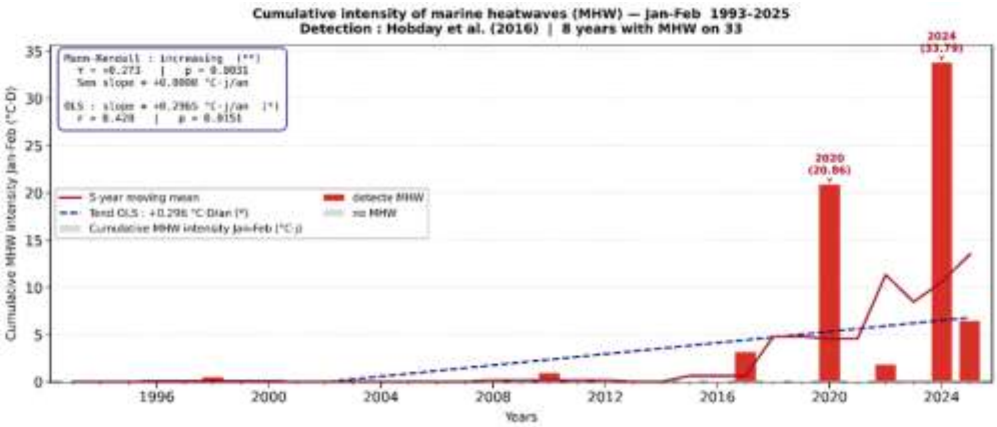

Fig. 3. Time series of the cumulative intensity of MHWs during the minor upwelling season from 1993 to 2025
The blue line represents the trend determined by the OLS test and the red curve represents the 5-year moving mean.

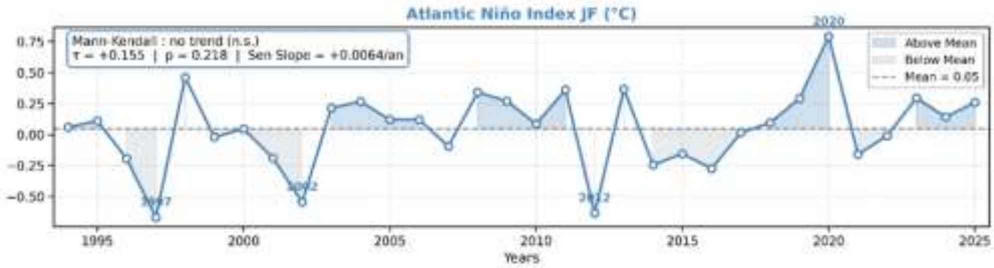

Fig. 4. Temporal pattern of the Atlantic El Niño from 1993 to 2025
The light blue area indicates values below the mean, and the blue area indicates values above the mean.

The 5-year moving average (red line) illustrates this shift in the thermal regime, moving from a historically neutral average level to an average value exceeding 10 °C.day by the end of the period. Similarly, statistical tests reveal a significant upward trend in the cumulative intensity of MHWs over the period 1993–2025. The slope of the trend line determined by the OLS test is +0.2965 °C.day/year, with r= 0.420 and p = 0.0151. This increase is statistically significant at α= 0.05 level. Furthermore, the non-parametric Mann-Kendall test confirms a monotonically increasing trend over the time series, with τ = +0.273 and p = 0.0031.

Fig. 4 shows the time series for the Atlantic Niño Index, calculated as an average over the two-month period January-February from 1994 to 2025. The positive anomalies, shown as blue areas, correspond to warm phases (Atlantic Niño), whilst the negative anomalies, shown as grey areas, correspond to cold phases (Atlantic Niña). The trend in the Atlantic Niño index curve shows several warm years, with 2020 recording the most extreme warm anomaly in the entire record, with a maximum value exceeding +0.75°C. Other significant peaks were observed in 1998, 2008, 2011 and 2013, with values of approximately 0.49°C, 0.35°C, 0.36°C and 0.37°C respectively. In addition to warm events, cold periods have also been observed, the most significant of which occurred in 1997 with a value of approximately -0.70°C. Other years recorded significant minimum peaks, such as 2002 and 2012, with respective values of approximately 0.51°C and 0.68°C. Statistical analysis of the Atlantic Niño Index, which has a mean of 0.05°C, shows no significant linear trend over the same period, with τ= +0.155 and p = 0.218. The Sen slope, with a value of +0.0064°C/year, confirms the absence of a secular drift.

Bivariate relationships between the Atlantic Niño, MHWs and the upwelling area

Fig. 5 show scatter plots relating the Atlantic Niño index, MHWs in January-February and the resurgent upwelling area during the same period. Observation of the spatial structure of the scatter plot in Fig. 5a reveals a high concentration of data points: approximately 70 per cent of the years analysed are clustered within a narrow core of distribution, ranging from X = -0.30°C to X = +0.4°C, corresponding to moderate upwelling areas ranging from 0 to 10.000 km², with the majority of zero-area values associated with Atlantic Niño indices greater than zero.

a

b

c

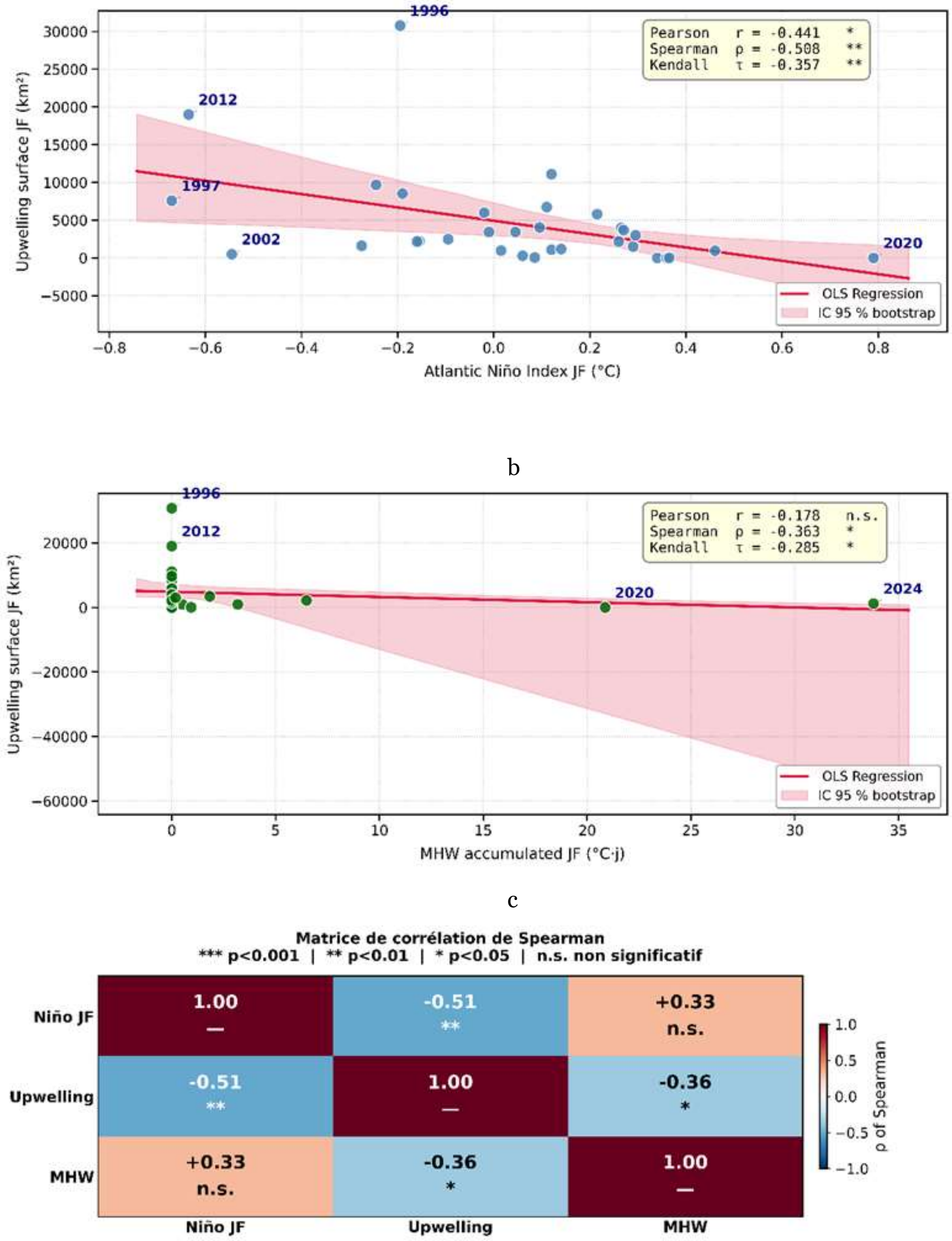

Fig. 5. Dispersion diagrams showing the relationship between the Atlantic Niño index and the upwelling surface (a), between the MHWs and the upwelling surface (b), and the correlogram of upwelling, the Atlantic Niño and the MHWs (c) for January-February from 1993 to 2025

However, the year 2020 lies at the far right of the graph, with the warmest index in the series approximately +0.79°C associated with a complete disappearance of the cold area, which was 0 km². In contrast, 2012 is situated in the top-left quadrant with an index of -0.63°C and a cold area of 19.000 km².

Furthermore, 1996 represents the highest anomaly in the 1993-2025 period. With a moderately cold index of approximately -0.21°C, the upwelling area reached the vertical peak of the series at 31,000 km², placing it well above the 95% uncertainty interval estimated by bootstrapping. In the lower left-hand quadrant, the year 2002 shows a remarkable divergence despite a pronounced Atlantic La Niña phase of -0.55°C, with the upwelling area remaining below 200 km². Similarly, the year 1997, although marking the absolute thermal minimum on record with an index of -0.67°C, developed only a moderate upwelling area of 7.500 km².

Statistically, Pearson's parametric test confirms a significant inverse linear relationship with $r = -0.441$ and $p < 0.05$. Nevertheless, the non-parametric Spearman's rank correlation coefficient of $\rho = -0.508$ ($p < 0.01$) and Kendall's rank correlation coefficient of $\tau = -0.357$ ($p < 0.01$) reach a higher level of significance. Furthermore, the OLS regression line (red line) indicates that the upwelling area decreases gradually as the Atlantic El Niño thermal anomaly intensifies.

Furthermore, the bivariate analysis between the upwelling area and the cumulative intensity of MHWs reveals a highly asymmetric distribution, dominated by a major concentration of observations with low thermal accumulations (Fig. 5b). The vast majority of years from 1993 to 2025 fall within a range of low upwelling area, between 0 and 10.000 km². Within this range, most data points cluster along the horizontal axis, showing zero or very low MHWs, generally between 0 and 6°C.day. However, extreme vertical outliers can be observed, represented by two key years 2020 and 2024. The year 2020 was marked by the complete disappearance of the upwelling area due to a strong thermal accumulation of approximately 21°C, whilst 2024 represents the absolute peak of the series in terms of MHW accumulation intensity approximately 34°C for a greatly reduced upwelling area of around 1200 km². Above 10.000 km², observations become extremely rare, reflecting the exceptional nature of events such as that observed in 2012, with a cold area of 19.000 km² and a cumulative MHW intensity of 0°C. d as well as in 1996, when the absolute maximum upwelling area for the entire series associated with a cold surface area of 31.000 km² and a cumulative MHW intensity of °C.day was observed.

Statistical analysis of this relationship using Pearson's linear correlation test did not yield a significant result ($r = -0.178$, $p > 0.05$). By contrast, Spearman's rank correlation ($\rho = -0.363$, $p < 0.05$) and Kendall's rank correlation ($\tau = -0.285$, $p < 0.05$) confirm the existence of a significant inverse relationship. Spearman's correlation matrix (Fig. 5c), which assesses the statistical relationships between the Atlantic El Niño, the upwelling area and the MHWs, shows negative correlations of -0.51 between the Atlantic El Niño and the upwelling area, and of -0.36 between the MHWs and the upwelling area. In terms of significance, only the correlation between the Atlantic El Niño and the upwelling area is significant.

Analysis of the dynamic causality of MHWs and the Atlantic Niño on the reduction in upwelling area

Fig. 6 assess the impact of MHWs and the Atlantic Niño on upwelling activity along the northern coast of the GoG during the minor upwelling season (January-February, 1993-2025). The analysis of the impact of MHWs on the upwelling area (Fig. 6a) reveals a strong and highly significant positive relationship, with a convergence correlation coefficient $r(L, \rho) = 0.99$ for $p < 0.001$. The cross-prediction coefficient ρ associated with $r(L, \rho)$ increases continuously with the library size L, rising from a value close to 0.09 for $L = 5$ to a maximum of 0.60 for $L = 25$.

Furthermore, the standard deviation of the bootstrap draws (yerr) increases slightly at high values of L due to the reduction in the size of the residual samples. At the same time, Fig. 6b of the analysis of the impact of the Atlantic Niño on the cold surface also shows a positive slope with $r(L, \rho) = 0.95$, where $p < 0.001$. The trend in ρ begins at negative values ($\rho = -0.02$ at $L = 5$) and then increases until it stabilises on a plateau between 0.28 and 0.32 for $L \geq 23$. Furthermore, the spatial distribution of the pixel-by-pixel Pearson correlation

Vol. 29, Issue: 2, p. 53-66, 2026

coefficient r between the cumulative intensity of MHWs and the cold surface (Fig. 6c) indicates that significant negative correlations predominate in the coastal zone and on the continental shelf, particularly between 7°W and 1°E, off the coasts of Ghana and Côte d'Ivoire, with values ranging from -0.32 to -0.16. Furthermore, the spatial distribution of the pixel-by-pixel Pearson correlation coefficient r between the Atlantic Niño and the cold surface (Fig. 6d) also shows a very marked negative correlation extending across the entire basin with r < -0.40, covering most of the offshore study area. The significant area ($p < 0.05$) is considerably larger and more contiguous than that of the MHWs.

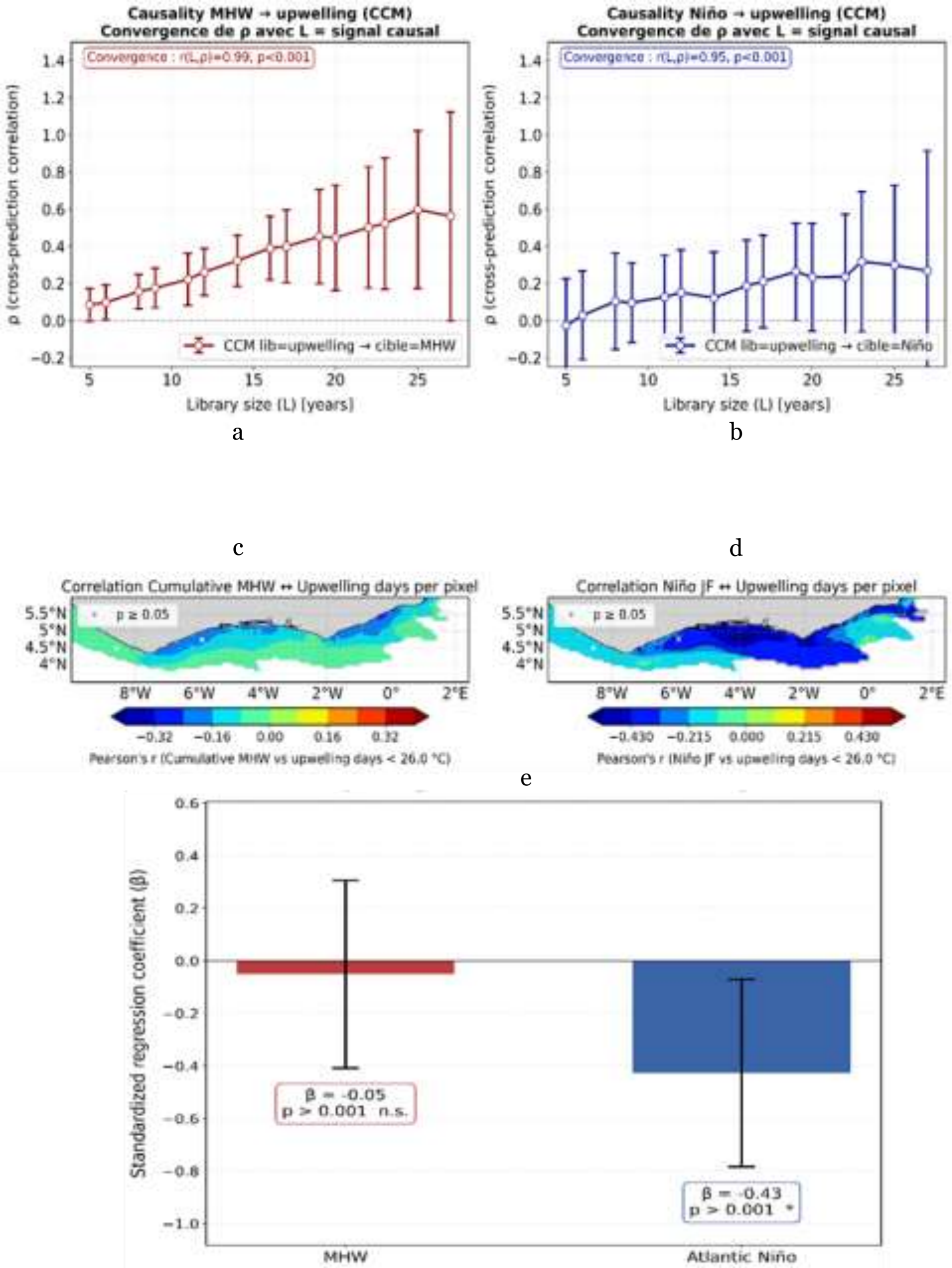

Fig. 6. (a) Causality diagram showing the relationship between MHWs and the upwelling area, (b) the relationship between the Atlantic El Niño and the upwelling area, (c) the spatial structure of the correlation between the cumulative intensity of MHWs and the upwelling area, (d) the spatial structure of the correlation between the Atlantic Niño and the upwelling area, and (e) the standardised regression coefficients (β) for the combined impact of MHWs and the Atlantic Niño on upwelling activity (January-February) from 1993 to 2025

Fig. 6e illustrates the standardised regression coefficients (β) derived from a multiple linear regression model assessing the simultaneous impact of MHWs and the Atlantic El Niño on upwelling activity (January–February). The overall coefficient of determination is $R^2 = 0.20$, indicating that the combined linear model explains 20 per cent of the interannual variance in upwelling. The standardised coefficient β for MHWs is -0.05, which is not statistically significant; its confidence interval, represented by the very wide error bar, overlaps the zero line considerably, ranging from -0.41 to +0.31. As for the standardised Atlantic El Niño coefficient for rang, extending from -0.78 to -0.07.

DISCUSSION

Our results provide an overview of the evolution of minor seasonal upwelling (January-February) along the northern coast of the GoG over the period 1993-2025, and of its sensitivity to the two climatic forcings, MHWs and the Atlantic Niño. Consequently, the climatological analysis of SST along the northern coast of the GoG confirms the existence of two distinct upwelling cells, separated at the longitude of Cape Three Points (~2.083°W), in line with the work of Djakouré *et al.* (2014) and Alory *et al.* (2021), who documented the presence of two major upwelling centres along the Ivorian and Ghanaian coasts. The western cell at Cape Palmas exhibits a more extensive cooling area than the eastern cell at Cape Three Points, suggesting spatial asymmetry. This spatial dichotomy may reflect the distinct mechanisms already documented for these two cells, with the Cape Three Points cell described as being predominantly driven by wind-induced alongshore Ekman transport, whilst the Cape Palmas cell responds more to the strengthening and detachment of the Guinea Current as well as to coastal mesoscale eddy activity (Djakouré *et al.*, 2014). Furthermore, the interannual variability of the Western Cell is characterised by extreme events such as that of 1996, when the cumulative area of upwelling exceeded 1.5×10^6 km²•days. This exceptional intensity can be put into perspective by the work of Illig *et al.* (2024), who show that equatorial Kelvin waves, driven by wind anomalies in the western equatorial basin, significantly control interannual fluctuations in sea level and subsurface temperature along the northern coast of the GoG. Thus, the 1996 event may have resulted from a particularly favourable combination of equatorial and local forcings. In contrast, the eastern cell shows a gradual and significant decline in its upwelling area, with an average loss of −3,559 km² day/year (p = 0.034), confirmed by Mann–Kendall tests (τ = -0.32, p = 0.009) and Pettitt tests (break in 2006-2007, p = 0.014). This negative trend contrasts with the absence of a significant trend observed for the western cell, suggesting that the two systems have different levels of vulnerability to recent environmental changes. Furthermore, an analysis of MHWs as defined by Hobday *et al.* (2016) reveals that major events are almost entirely concentrated after 2017, with a record peak in 2024 (33.9 °C.day). This trend is consistent with the findings of Koné *et al.* (2022), who documented an increase in the frequency of MHWs since 2015 along the northern coast of the GoG. Similarly, Djakouré *et al.* (2023) showed that the eastern tropical Atlantic has experienced an average of two MHW events per year over recent decades, with a more marked increase along the northern coast of the GoG than in other areas.

The significant upward trend in the cumulative intensity of MHWs (OLS slope of +0.2965 °C.day/year, p= 0.0151) confirms accelerated warming of surface waters. The 5-year moving average illustrates a thermal shift from a historically neutral period to a recent phase in which the cumulative intensity exceeds 10 °C.day. This trend is consistent with climate change projections, which predict an intensification of extreme heat events in tropical regions (Oliver *et al.*, 2019).

Analysis of the relationship between the Atlantic Niño and the cold surface revealed significant negative correlations between the Atlantic Niño index and the upwelling area (Pearson r = -0.441, $p < 0.05$; Spearman's ρ = -0.508, $p < 0.01$), confirming that warm phases of the Atlantic Niño are associated with a reduction in coastal upwelling. These results are consistent with the work of Djakouré *et al.* (2014), who showed that the Equatorial Atlantic Mode influences the intensity of summer upwelling in the GoG. The year 2020, characterised by the most extreme Atlantic Niño warm anomaly (+0.79°C) and a complete disappearance of the upwelling area, perfectly illustrates this mechanism. However, the relationship between MHWs and the upwelling area is not significant according to Pearson's test (r = -0.178, $p > 0.05$) and is confirmed by Spearman's rank test (ρ = −0.363, $p < 0.05$) and Kendall's rank test (τ = -0.285, $p < 0.05$). However, the asymmetric distribution of the observations, with extreme vertical outliers in 2020 and 2024, suggests that the most intense MHWs coincide with very small upwelling areas.

This is consistent with the studies by Koné *et al.* (2022), who also observed that the variability in MHWs is consistent with ocean warming and a reduction in the upwelling area. Similarly, the dynamic causality analysis using convergent cross-mapping reveals a significant influence of both MHWs (r = 0.99, $p < 0.001$) and the Atlantic Niño (r = 0.95, $p < 0.001$) on the upwelling area. The high convergence correlation coefficients indicate a robust causal relationship, suggesting that both phenomena act as independent but convergent forcings on upwelling activity. Furthermore, spatial correlation maps show that the Atlantic El Niño exerts a more widespread influence across the entire basin (r < -0.40) than MHWs, whose impact is more confined to the coastal band between 7°W and 1°E. This difference in spatial footprint suggests that the Atlantic El Niño acts as a large-scale forcing, whilst MHWs have a more localised impact, likely linked to coastal air-sea coupling processes. Thus, our results indicate, based on the multiple regression model, that the Atlantic Niño is the main explanatory factor for the reduction in upwelling during the minor cold season (standardised β = -0.43, significant), whilst the effect of MHWs alone is not significant (β= -0.05). This result highlights that the Atlantic Niño acts as a major forcing, potentially through changes to the thermocline and surface winds, whilst MHWs may be partly a consequence of the latter rather than an independent cause. The work by Illig *et al.* (2024) has also shown that coastal variability in the GoG is primarily controlled by equator-driven waves, leaving a marginal role for local forcing.

CONCLUSION

In summary, this study highlights a marked contrast between the two upwelling cells in the northern GoG: the western cell exhibits high interannual variability with no significant trend, whilst the eastern cell has undergone a gradual and statistically robust decline since a regime shift that occurred between 2006 and 2007. At the same time, the almost exclusive occurrence of MHWs since 2017, with record intensities in 2020 and 2024, attests to a major recent thermal shift in the region. Statistical and causal analyses show that the Atlantic El Niño is the main driver of the reduction in upwelling, acting on a large scale, whilst the direct impact of MHWs appears to be more localised and may be partly a consequence of the weakening of upwelling rather than an independent cause. These results highlight the need for a regionalised approach to the management of marine resources and fisheries, in the face of increasingly vulnerable dynamic systems. They also call for the strengthening of observation networks and regional models, in order to improve inter-annual forecasting of coastal conditions and to anticipate the ecological and socio-economic impacts on West African populations.

ACKNOWLEDGEMENTS

The authors would like to thank the anonymous reviewers for their valuable comments and suggestions to improve the quality of the paper.

REFERENCES

Alory G, Da-Allada CY, Djakouré S, Dadou I, Jouanno J, Loemba DP. 2021. Coastal upwelling limitation by onshore geostrophic flow in the Gulf of Guinea around the Niger River plume. Frontiers in Marine Science **7**, 607216.

Bakun A. 1978. Guinea current upwelling. Nature **271**, 147–150.

Brandt P, Alory G, Awo FM, Dengler M, Djakouré S, Imbol Koungue RA, Jouanno J, Körner M, Roch M, Rouault M. 2023. Physical processes and biological productivity in the upwelling regions of the tropical Atlantic. Ocean Science **19**, 581–601.

Caniaux G, Giordani H, Redelsperger J-L, Guichard F, Key E, Wade M. 2011. Coupling between the Atlantic cold tongue and the West African monsoon in boreal spring and summer. Journal of Geophysical Research **116**, C04003. DOI: 10.1029/2010JC006570

Demarcq H, Aman A. 2002. A multi-data approach for assessing the spatio-temporal variability of the Ivorian-Ghanaian coastal upwelling: Understanding pelagic fish stock dynamics. In: Large Marine Ecosystems **11**, Elsevier, 83–xxxiii.

Djakouré S, Kone M, Koffi KU, Kouadio KY, Adon M, Nyadjro E, Ta S. 2023. Characterization of marine heat waves in the eastern tropical Atlantic Ocean. Frontiers in Marine Science **10**, 1293779.

Djakouré S, Penven P, Bourlès B, Veitch J, Koné V. 2014. Coastally trapped eddies in the north of the Gulf of Guinea. JGR Oceans **119**, 6805–6819. DOI: 10.1002/2014JC010243

Hardman-Mountford NJ, McGlade JM. 2003. Seasonal and interannual variability of oceanographic processes in the Gulf of Guinea: An investigation using AVHRR sea surface temperature data. International Journal of Remote Sensing **24**, 3247–3268. DOI: 10.1080/0143116021000021297

Hipel KW, McLeod AI. 1994. Time series modelling of water resources and environmental systems. Elsevier.

Hobday AJ, Alexander LV, Perkins SE, Smale DA, Straub SC, Oliver ECJ, Benthuysen JA, Burrows MT, Donat MG, Feng M, Holbrook NJ, Moore PJ, Scannell HA, Sen Gupta A, Wernberg T. 2016. A hierarchical approach to defining marine heatwaves. Progress in Oceanography **141**, 227–238. DOI: 10.1016/j.pocean.2015.12.014

Houghton RW. 1989. Influence of local and remote wind forcing in the Gulf of Guinea. Journal of Geophysical Research **94**, 4816–4828. DOI: 10.1029/JC094iC04p04816

Illig S, Djakouré S, Mitchodigni T. 2024. Influence of the remote equatorial dynamics on the interannual variability along the northern coast of the Gulf of Guinea. JGR Oceans **129**, e2024JC021011. DOI: 10.1029/2024JC021011

Imbol Koungue RA, Illig S, Rouault M. 2017. Role of interannual Kelvin wave propagations in the equatorial Atlantic on the Angola Benguela Current system. JGR Oceans **122**, 4685–4703. DOI: 10.1002/2016JC012463

Jean-Michel L, Eric G, Romain B-B, Gilles G, Angélique M, Marie D, Clément B, Mathieu H, Olivier LG, Charly R. 2021. The Copernicus global 1/12 oceanic and sea ice GLORYS12 reanalysis. Frontiers in Earth Science **9**, 698876.

Jouanno J, Hernandez O, Sanchez-Gomez E. 2017. Equatorial Atlantic interannual variability and its relation to dynamic and thermodynamic processes. Earth System Dynamics **8**, 1061–1069.

Koné M, Djakouré S, Adon M, Ta S, Kouadio Y. 2022. Marine heatwaves, upwelling, and atmospheric conditions during the monsoon period at the northern coast of the Gulf of Guinea. Climate **10**, 199.

Koné M, Kouadio YK, Adon M. 2025. Relationship between Tropical Atlantic marine heatwaves and rainfall in West Africa during the monsoon period. Advances in Meteorology **2025**, 7899901. DOI: 10.1155/adme/7899901

Kouadio YK, Djakouré S, Aman A, Ali KE, Koné V, Toualy E. 2013. Characterization of the boreal summer upwelling at the northern coast of the Gulf of Guinea based on the PROPAO in situ measurements network and satellite data. International Journal of Oceanography **2013**.

Mallakpour I, Villarini G. 2016. A simulation study to examine the sensitivity of the Pettitt test to detect abrupt changes in mean. Hydrological Sciences Journal **61**, 245–254. DOI: 10.1080/02626667.2015.1008482

Nubi O, Oyatola OO, Bonou F. 2019. Spatial variability in autumnal equatorial upwelling intensity within the Gulf of Guinea as inferred from in situ measurements. Journal of Oceanography and Marine Science **10**, 1–10.

Oliver EC, Burrows MT, Donat MG, Sen Gupta A, Alexander LV, Perkins-Kirkpatrick SE, Benthuysen JA, Hobday AJ, Holbrook NJ, Moore PJ. 2019. Projected marine heatwaves in the 21st century and the potential for ecological impact. Frontiers in Marine Science **6**, 734.

Oliver EC, Perkins-Kirkpatrick SE, Holbrook N, Bindoff N. 2018. Anthropogenic and natural influences on record 2016 marine heat waves.

Osada Y, Ushio M, Kondoh M. 2023. Unified understanding of nonparametric causality detection in time series. DOI: 10.1101/2023.04.20.537743

Runge J, Nowack P, Kretschmer M, Flaxman S, Sejdinovic D. 2019. Detecting and quantifying causal associations in large nonlinear time series datasets. Science Advances **5**, eaau4996. DOI: 10.1126/sciadv.aau4996

Song Q, Aiki H. 2023. Equatorial wave diagnosis for the Atlantic Niño in 2019 with an ocean reanalysis. Ocean Science **19**, 1705–1717.

Stock JH, Watson MW. 2017. Twenty years of time series econometrics in ten pictures. Journal of Economic Perspectives **31**, 59–86.

Sugihara G, May R, Ye H, Hsieh C, Deyle E, Fogarty M, Munch S. 2012. Detecting causality in complex ecosystems. Science **338**, 496–500. DOI: 10.1126/science.1227079

Tan W, Liu Y, Li X, Johnson NC, Hu Z-Z. 2023. Multi-time scale variations in Atlantic Niño and a relative Atlantic Niño index. Geophysical Research Letters **50**, e2023GL106511.

Wernberg T. 2021. Marine heatwave drives collapse of kelp forests in Western Australia. In: Ecosystem Collapse and Climate Change **241**, 325–343. DOI: 10.1007/978-3-030-71330-0_12

Wooldridge JM. 2016. Introductory econometrics: A modern approach. South-Western Cengage Learning.

Xie H, Li D, Xiong L. 2014. Exploring the ability of the Pettitt method for detecting change point by Monte Carlo simulation. Stochastic Environmental Research and Risk Assessment **28**, 1643–1655. DOI: 10.1007/s00477-013-0814-y